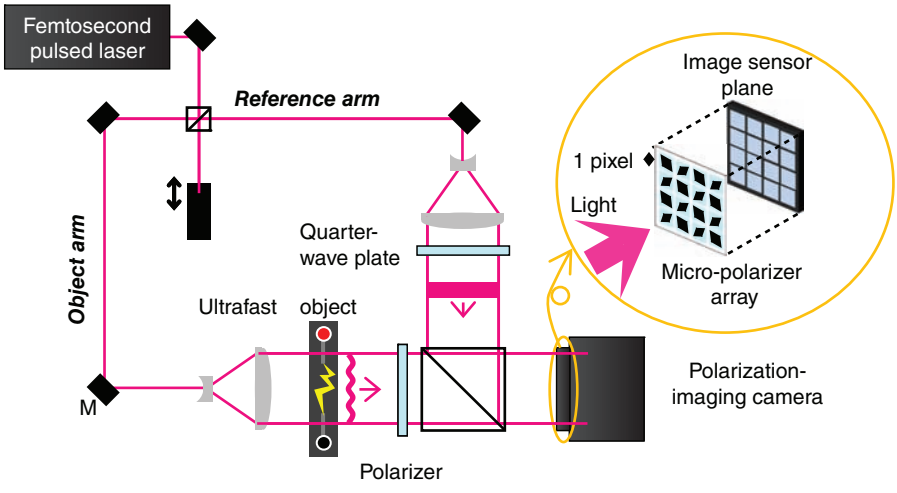

Plate 1 (Figure 1.13) Schematic diagram of parallel phase-shifting digital holography system using a femtosecond pulsed laser

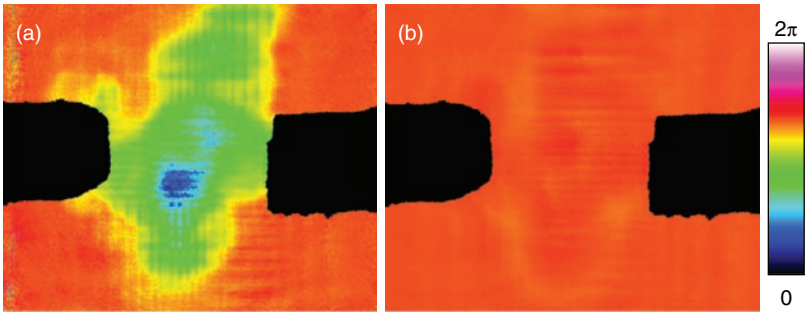

Plate 2 (Figure 1.15) Reconstructed images. (a) By parallel phase-shifting digital holography, (b) by a diffraction integral alone

Multi-dimensional Imaging, First Edition. Edited by Bahram Javidi, Enrique Tajahuerce and Pedro Andrés.

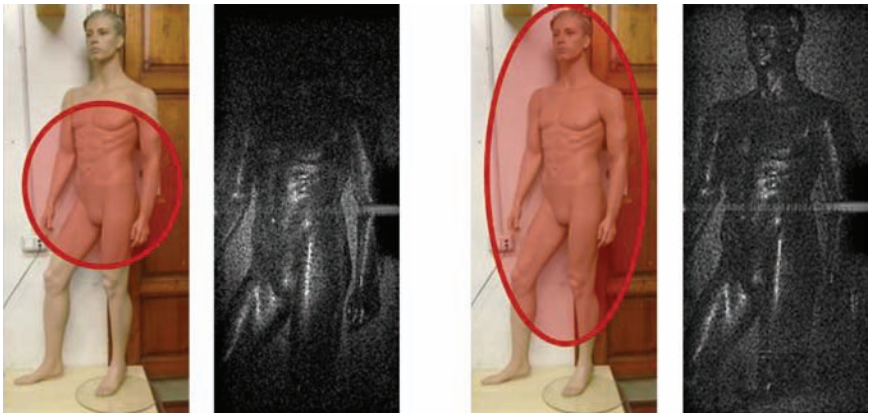

Plate 3 (Figure 2.9) (a) Spherical lens configuration. Mannequin image with irradiated area in red; mannequin hologram amplitude reconstruction. (b) Cylindrical lens configuration. Mannequin image with irradiated area in red; mannequin hologram amplitude reconstruction

Plate 4 (Figure 2.10) (From left to right) Mannequin image with irradiated area in red; mannequin hologram amplitude reconstruction at different scanning time and superposition of the most significant frames

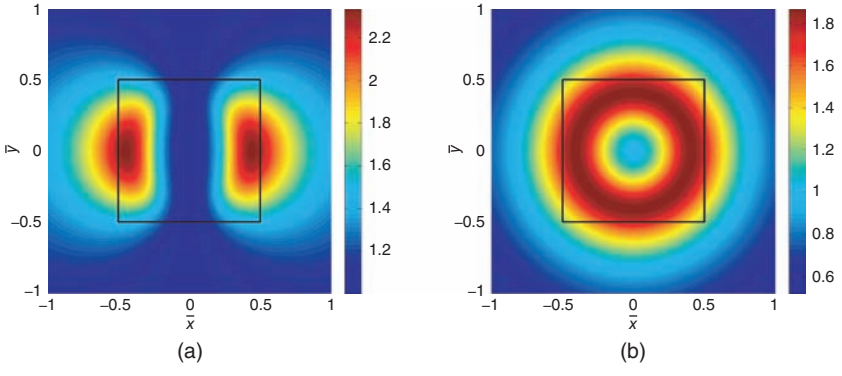

Plate 5 (Figure 3.10) Single point resolution in a transversal plane (from Fournier *et al*. 2010): (a) x-resolution map normalized by the value of x-resolution on the optical axis; (b) normalized z-resolution map. The squares in the center of figures (a) and (b) represent the sensor boundaries. *Source*: Fournier C., Denis L., and Fournel T., 2010. Reproduced with permission from the Optical Society

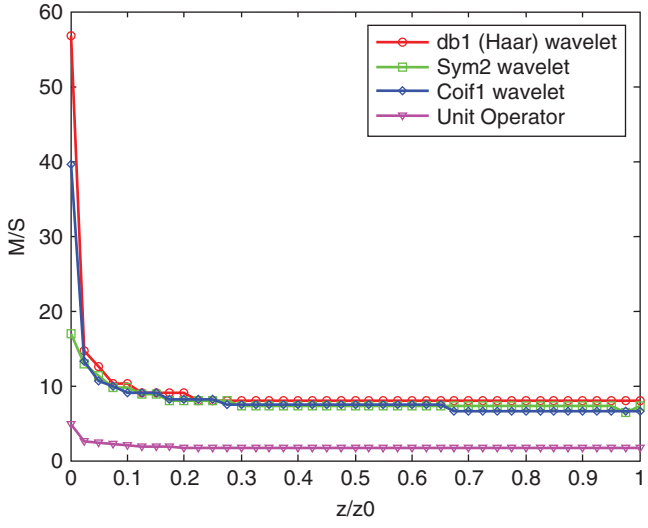

Plate 6 (Figure 4.6) Simulation results showing the normalized compressive sampling ratio for different sparsifying bases [26]. *Source*: Y. Rivenson, A. Stern, and B. Javidi 2013. Reproduced with permission from The Optical Society

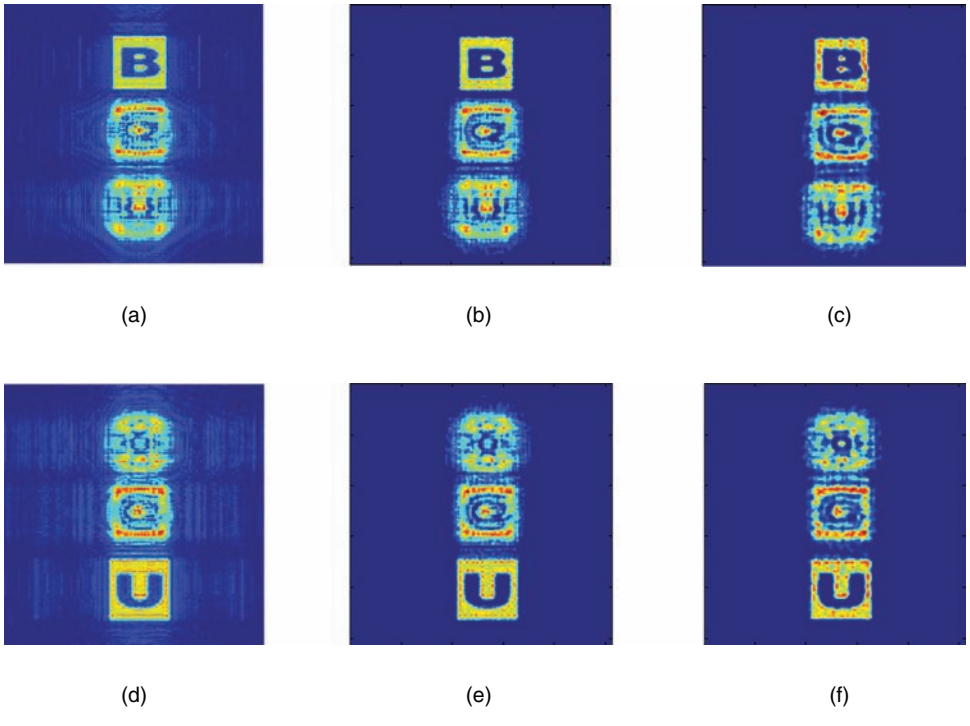

Plate 7 (Figure 4.9) Reconstruction examples of the B (forward) and U (backward) planes. (a) Reconstruction of the B plane form 100% of the projections. (b) CS reconstruction of the B plane forms 6% of the projections. (c) CS reconstruction of the B plane forms 2.5% of the projections. (d) Reconstruction of the U plane forms 100% of the projections. (e) CS reconstruction of the U plane forms 6% of the projections. (f) CS reconstruction of the U plane forms 2.5% of the projections

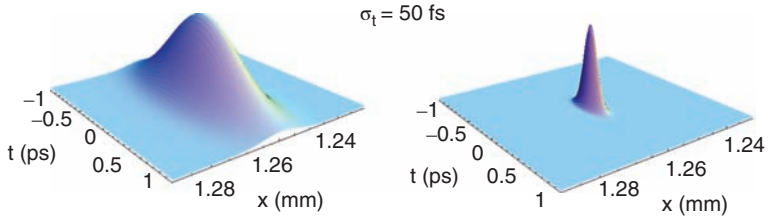

Plate 8 (Figure 5.6) Spatiotemporal profiles of the fifth diffraction order of a 100 lines/inch diffractive grating for an input pulse width of $\sigma_t = 50$ fs. The right part of the figure is obtained after focusing with an achromatic lens doublet and the left part by focusing with the DOE-based system. Note that the time origin is chosen arbitrarily. *Source*: Mínguez-Vega, G., Tajahuerce, E., Fernández-Alonso, M., Climent, V., Lancis, J., Caraquitena, J., Andrés, P., (2007). Figure 6. Reproduced with permission from The Optical Society

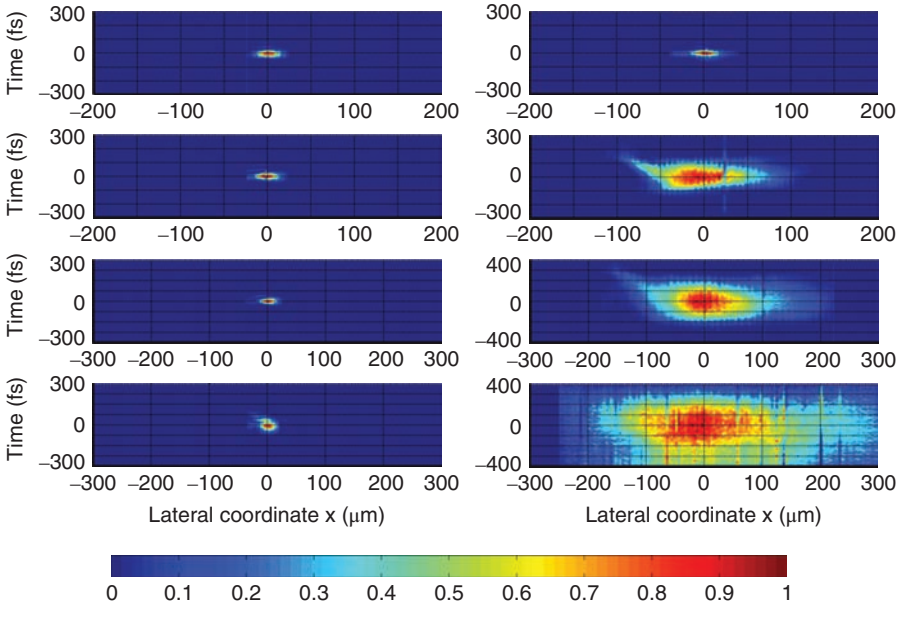

Plate 9 (Figure 5.9) Normalized spatiotemporal light intensity after low NA focusing of the beamlets coming from a diffractive grating (0th, +1st, +2nd, and +3rd diffraction orders from *top to bottom*) with (*left column*) and without (*right column*) DCM. Measurements were captured using STARFISH [18]. The maximum frequency component, for the third diffraction order, is 35.4 lp/mm. *Source*: Martínez-Cuenca, R., Mendoza-Yero, O., Alonso, B., Sola, Í. J., Mínguez-Vega, G., Lancis, J. (2012). Figure 2. Reproduced with permission from The Optical Society

Plate 10 (Figure 6.6) (a) Out of focus color intensity of the alga *Odontella* sp., (b) refocused intensity, (c) composite phase image of the RGB channels

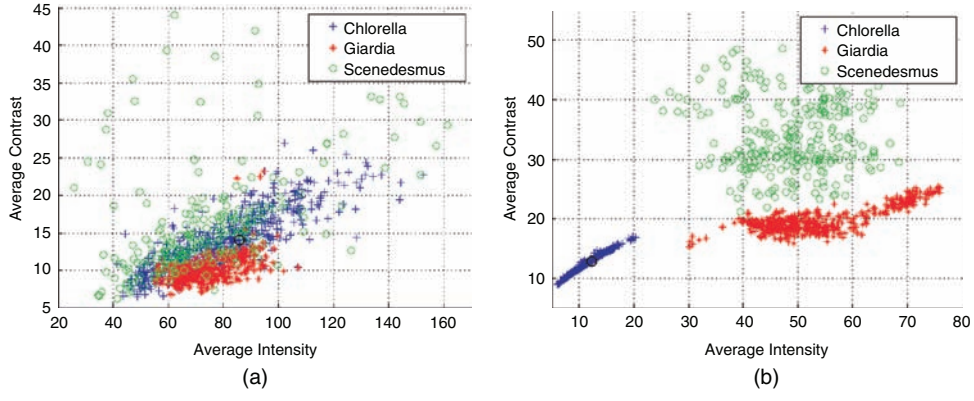

Plate 11 (Figure 6.13) Feature space representation using (a) intensity information of the detected particles of the three species, and (b) compensated phase of detected particles of the three species

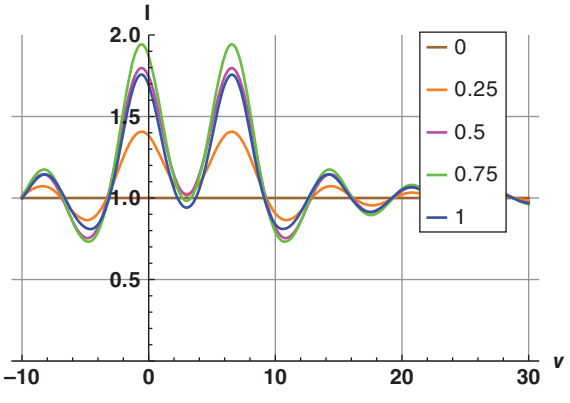

Plate 12 (Figure 7.14) Imaging of two neighboring point-like phase defects using VDIC with different parameters

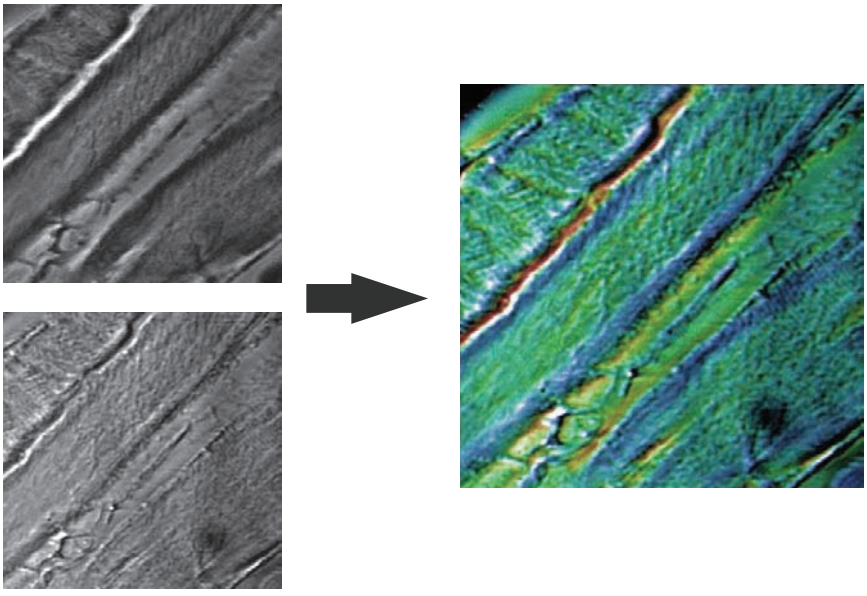

Plate 13 (Figure 7.15) Combination of an image obtained using Zernike phase contrast (hue) and one obtained using DIC (intensity) in order to visualize a phase structure

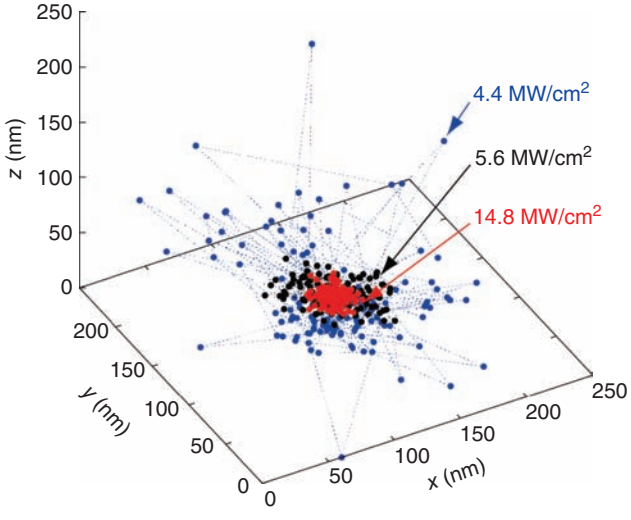

Plate 14 (Figure 8.7) Movement of a 200 nm polystyrene particle in the trapping volume at different intensities: (blue) 4.4 MW/cm^2, (black) 5.6 MW/cm^2, and (red) 14.8 MW/cm^2

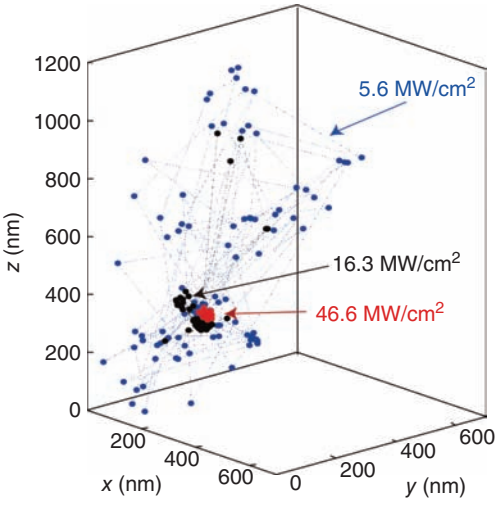

Plate 15 (Figure 8.10) Three-dimensional display of the gold nanoparticle movements

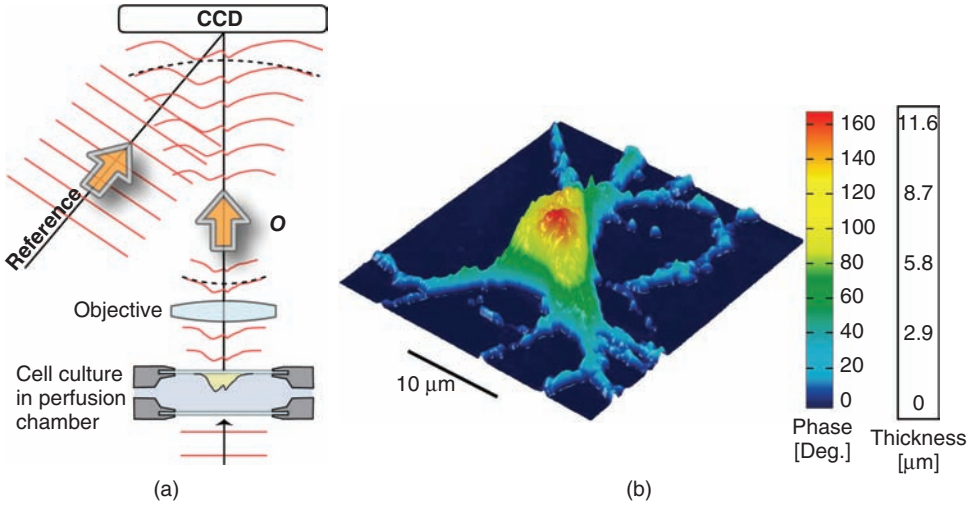

Plate 16 (Figure 9.2) Digital holographic microscopy (DHM) of living mouse cortical neurons in culture. (a) Schematic representation of cultured cells mounted in a closed perfusion chamber and trans-illuminated (b) 3D perspective image in false colors of a living neuron in culture. Each pixel represents a quantitative measurement of the phase retardation or cellular optical path length (OPL) induced by the cell with a sensitivity corresponding to a few tens of nanometers. By using the measured mean value of the neuronal cell body refractive index, resulting from the decoupling procedure, scales (*right*), which relate OPL (°) to morphology in the *z*-axis (µm), can be constructed

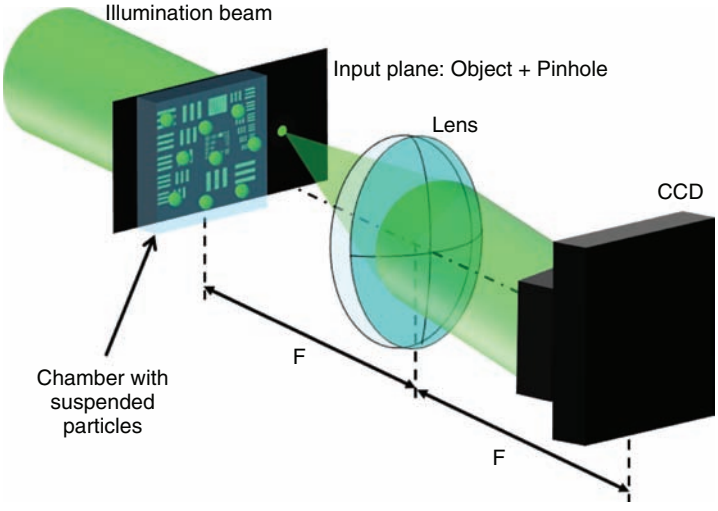

Plate 17 (Figure 10.4) Digital holography super-resolution setup. *Source*: Zalevsky Z., Gur E., Garcia J., Micó V., Javidi B. 2012. Figure 1. Reproduced with permission from The Optical Society

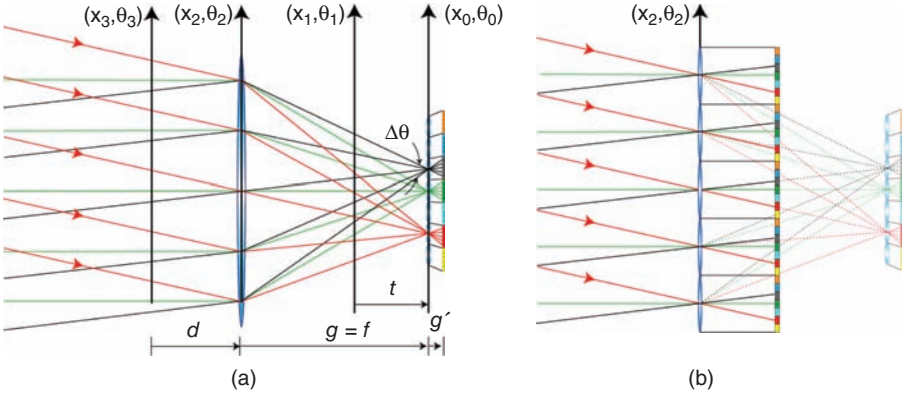

Plate 18 (Figure 11.17) (a) Scheme for the calculation of the plenoptic function in planes parallel to the MLA; (b) the plenoptic field as evaluated in the plane of the camera lens is equivalent to the one captured with an IP setup

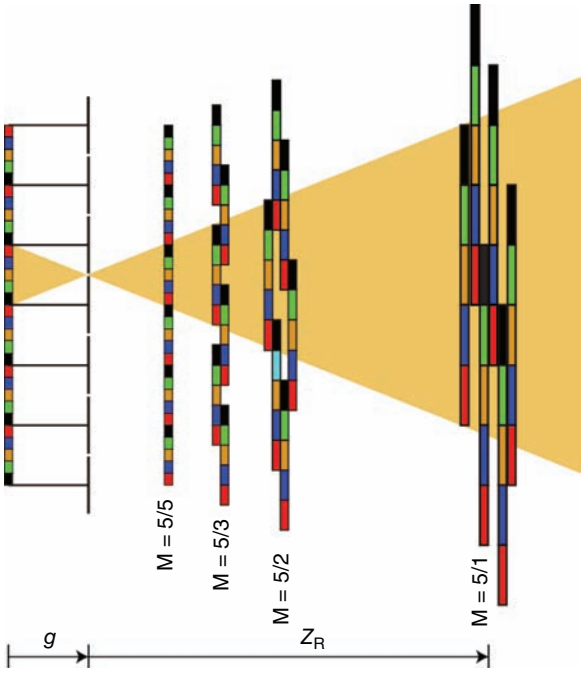

Plate 19 (Figure 11.20) Scheme of the conventional reconstruction algorithm. In this figure, the number of pixels per microlens is $N = 5$

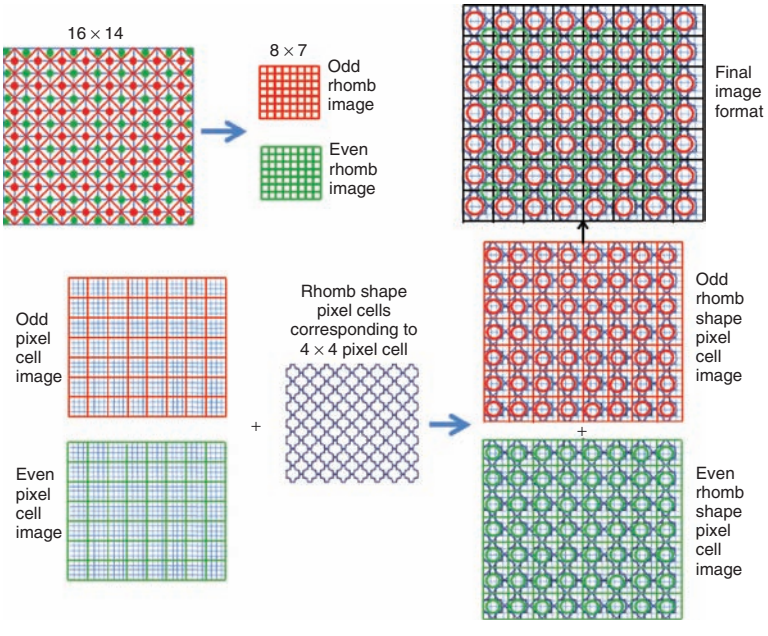

Plate 20 (Figure 12.12) The image format of the rhombus cell corresponding to a pixel cell with 4×4 pixels

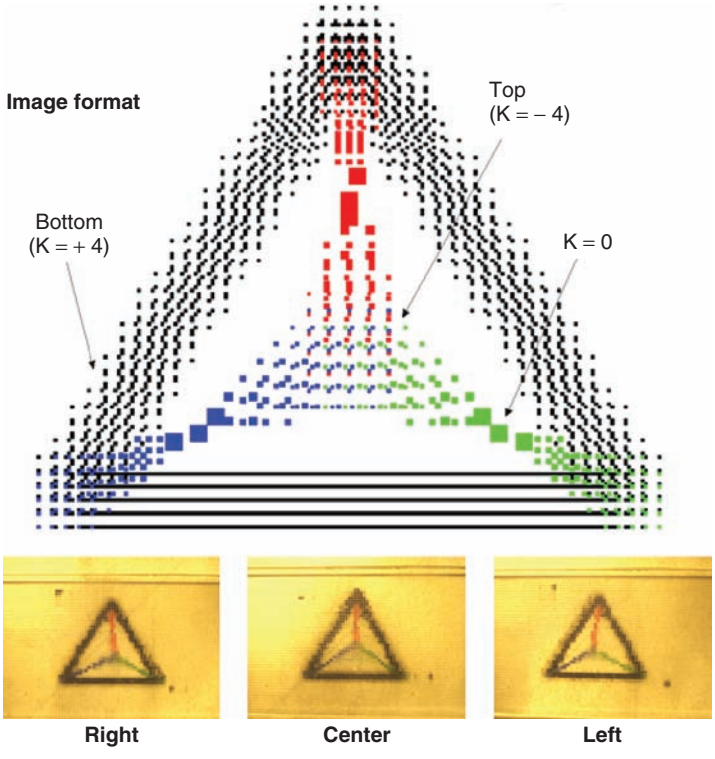

Plate 21 (Figure 12.16) Image format of a triangular pyramid

(b)

Plate 22 (Figure 13.8) Reconstruction of FP-HS. (b) Example of the reconstructed image from full-color FP-HS hologram [20]. *Source*: T. Utsugi and M. Yamaguchi 2013. Reproduced with permission from The Optical Society

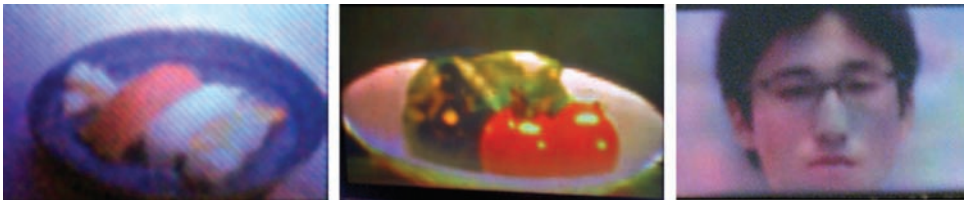

(a) (b) (c)

Plate 23 (Figure 13.23) Reconstructed images from the FP HS recorded from the captured light-field data. (a) Sushi, (b) vegetables, and (c) human face

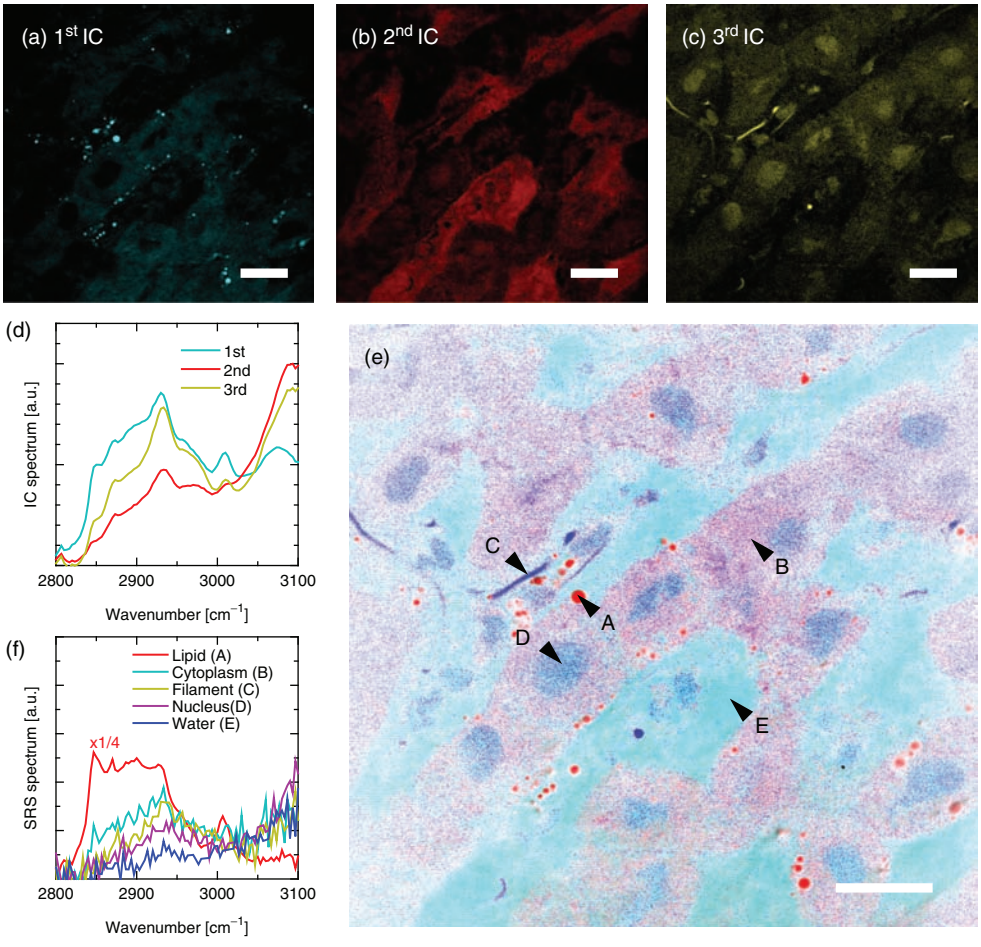

Plate 24 (Figure 15.12) Spectral imaging of a rat liver tissue [28]. 91 images at wavenumbers from 2800–3100 cm^{-1} were taken and averaged over 10 times. The total acquisition time was <30 s. The spectral images were analyzed by using 5 ICs. (a) First IC image reflecting the distribution of lipid-rich region. (b) Second IC image reflecting the distribution of water-rich regions. (c) Third IC image reflecting the distribution of protein-rich region. (d) IC spectra. (e) Multicolor image produced by combining images (a–c) and inverting the contrast. (a)–(e) are explained in the text. (f) SRS spectra in locations indicated by arrows in (e). Scale bar: 20 µm. *Source*: Y. Ozeki, W. Umemura, Y. Otsuka, S. Satoh, H. Hashimoto, K. Sumimura, N. Nishizawa, K. Fukui, and K. Itoh 2012. Reproduced with permission from Nature Publishing

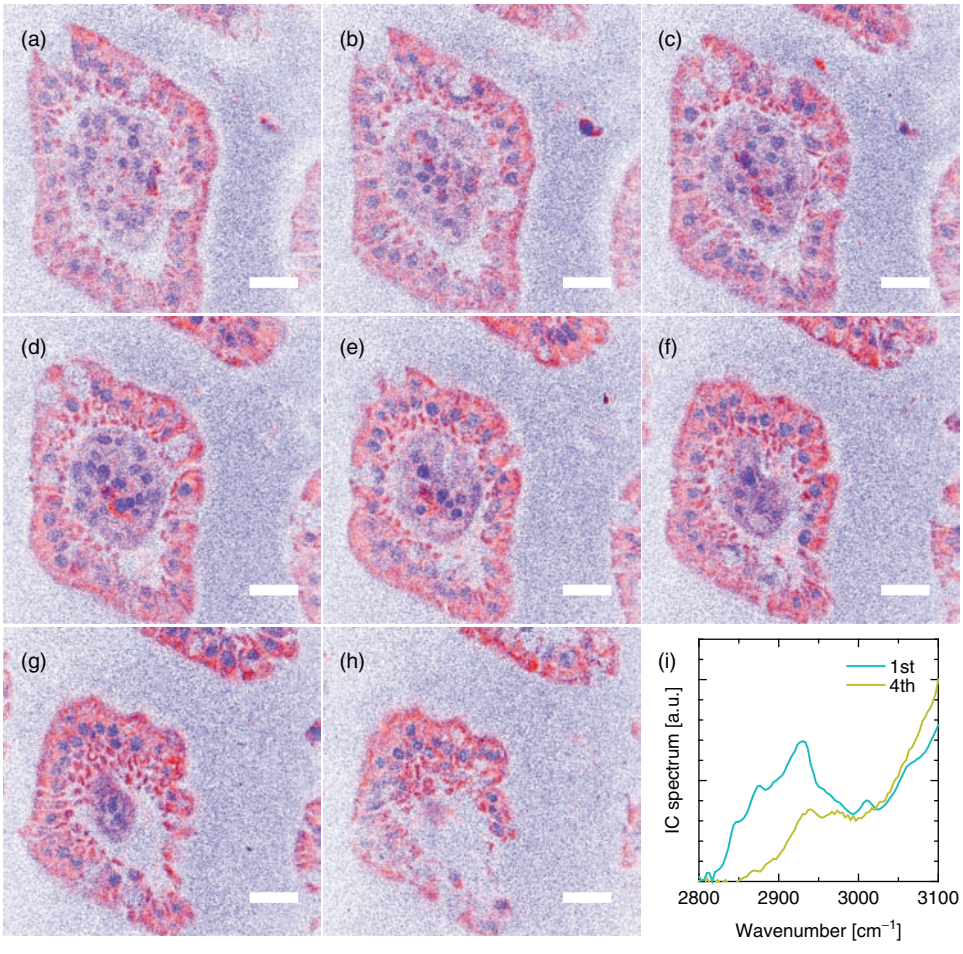

Plate 25 (Figure 15.13) Sectioned spectral imaging of intestinal villi in the mouse [28]. 91 images at wavenumbers from 2800–3100 cm^{-1} were taken by changing the z position by 5.6 µm. The total acquisition time was 24 s. The spectral images were analyzed by using 4 ICs. The first IC (cytoplasm) and the fourth IC (nuclei) images were colored cyan and yellow, respectively, and then combined and the contrast was inverted. (a–h). Sectioned multicolor images. (f). Spectra of the first and fourth ICs. Scale bar: 20 µm. *Source*: Y. Ozeki, W. Umemura, Y. Otsuka, S. Satoh, H. Hashimoto, K. Sumimura, N. Nishizawa, K. Fukui, and K. Itoh 2012. Reproduced with permission from Nature Publishing

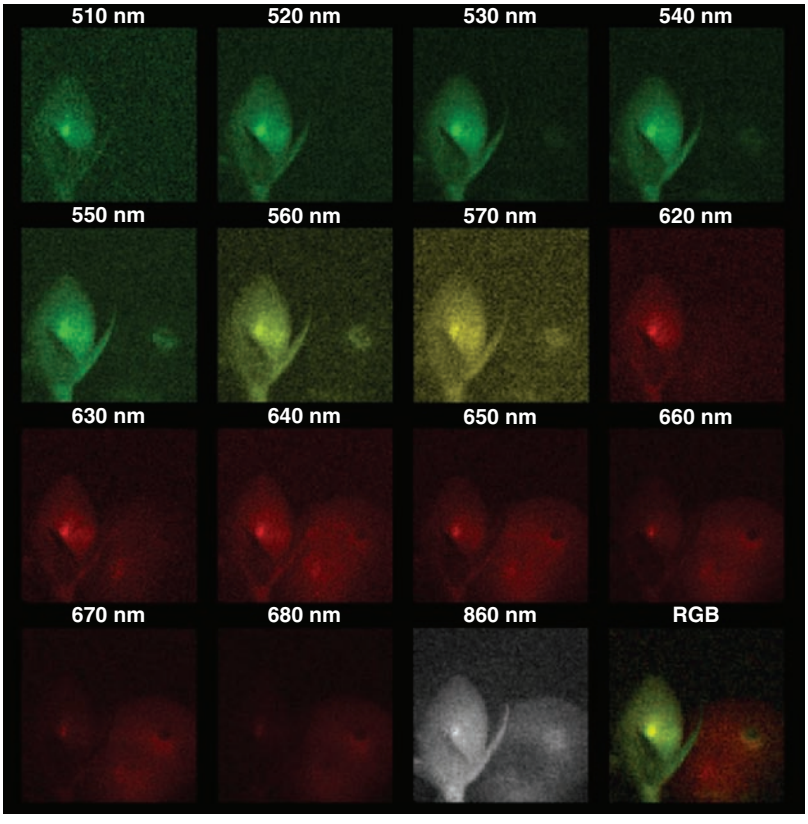

Plate 26 (Figure 16.5) Multispectral data cube reconstructed using CS. In the VIS band, the reflectance for each spectral channel is represented by means of a 256×256 pseudo-color image. In the NIR band we show a gray-scale representation. A colorful image of the scene made up from the conventional RGB channels is also included. *Source*: F. Soldevila, E. Irles, V. Durán, P. Clemente, M. Fernández-Alonso, E. Tajahuerce, and J. Lancis 2013, Figure 4. Reproduced with permission from Springer

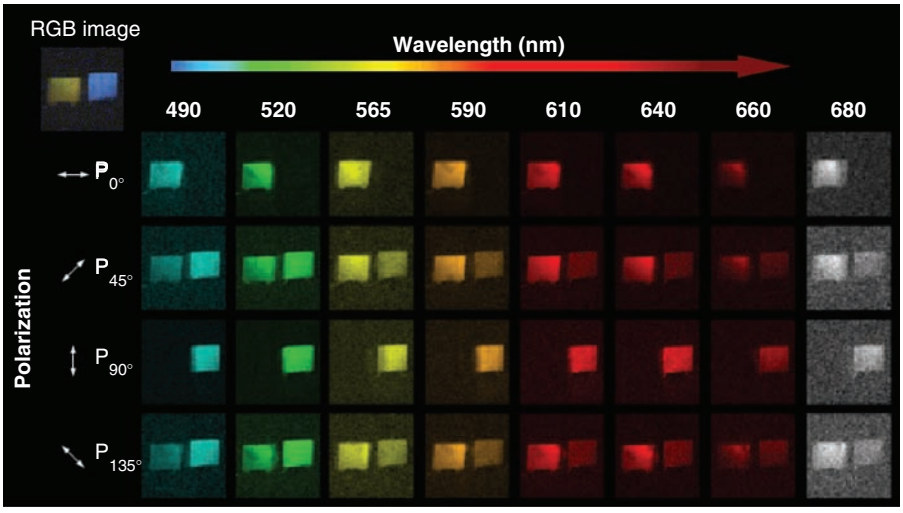

Plate 27 (Figure 16.8) Multispectral image cube reconstructed by CS algorithm for four different configurations of the polarization analyzer. The RGB image of the object is also included. In the VIS spectrum all channels are represented by pseudo-color images and a gray-scale representation is used for the wavelength closer to the NIR spectrum. *Source*: F. Soldevila, E. Irles, V. Durán, P. Clemente, M. Fernández-Alonso, E. Tajahuerce, and J. Lancis 2013, Figure 5. Reproduced with permission from Springer

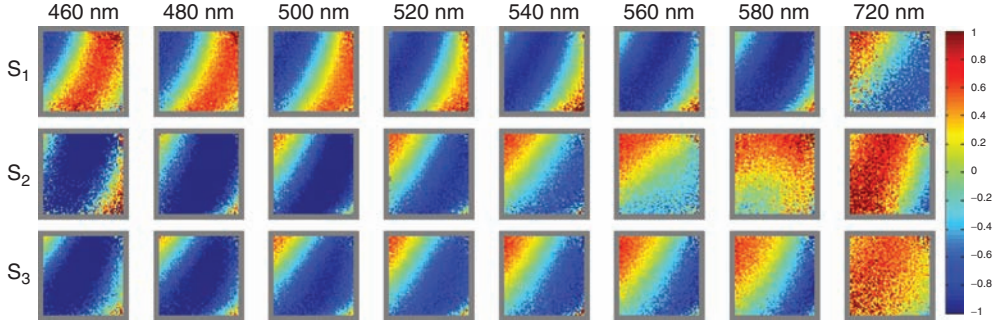

Plate 28 (Figure 16.11) Spatial distribution of the Stokes parameters of the polystyrene piece. Each distribution is represented by a pseudo-colored 128 × 128 pixels picture. The values range from −1 (blue) to 1 (red)

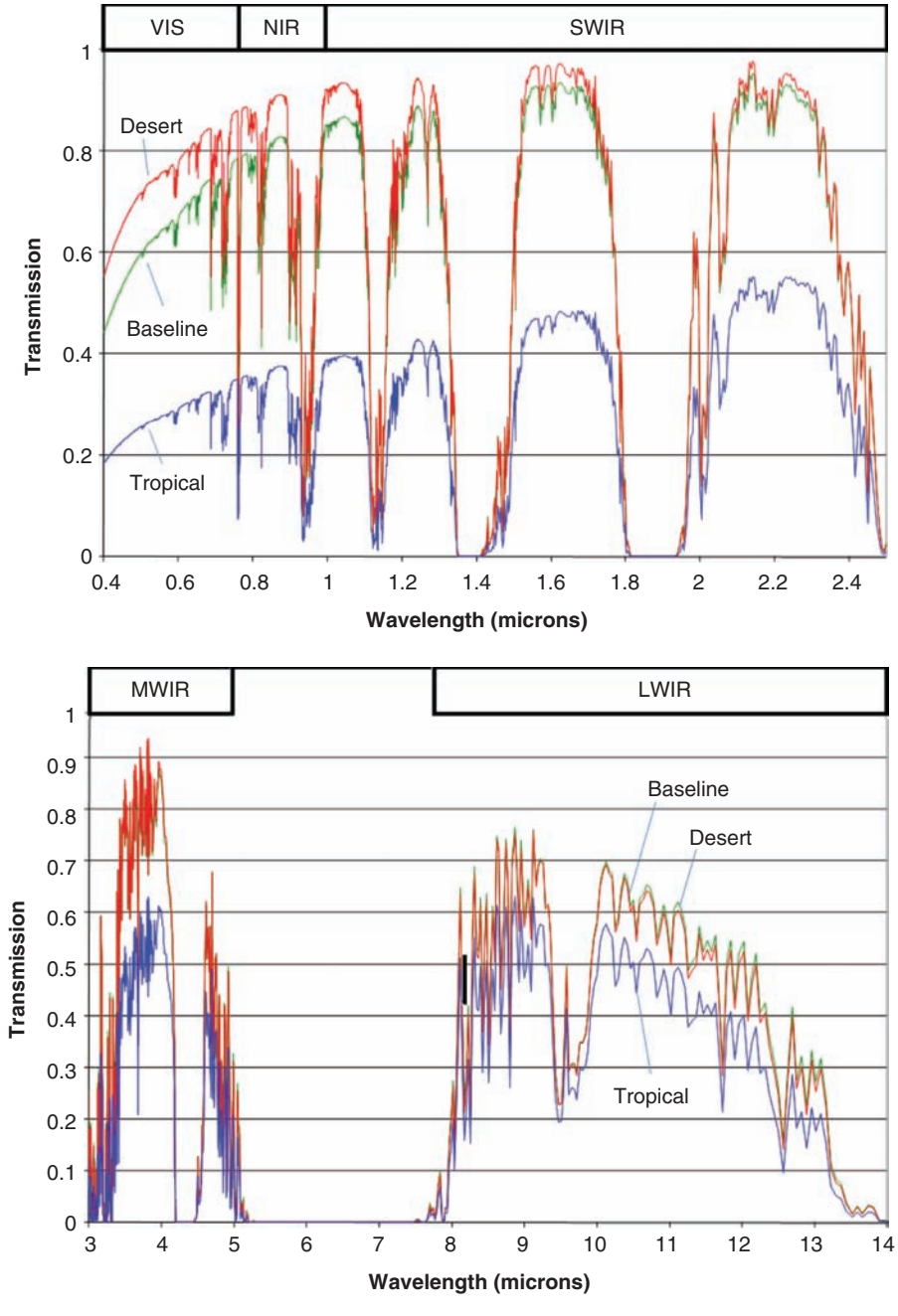

Plate 29 (Figure 17.11) Ground to space atmospheric transmission windows

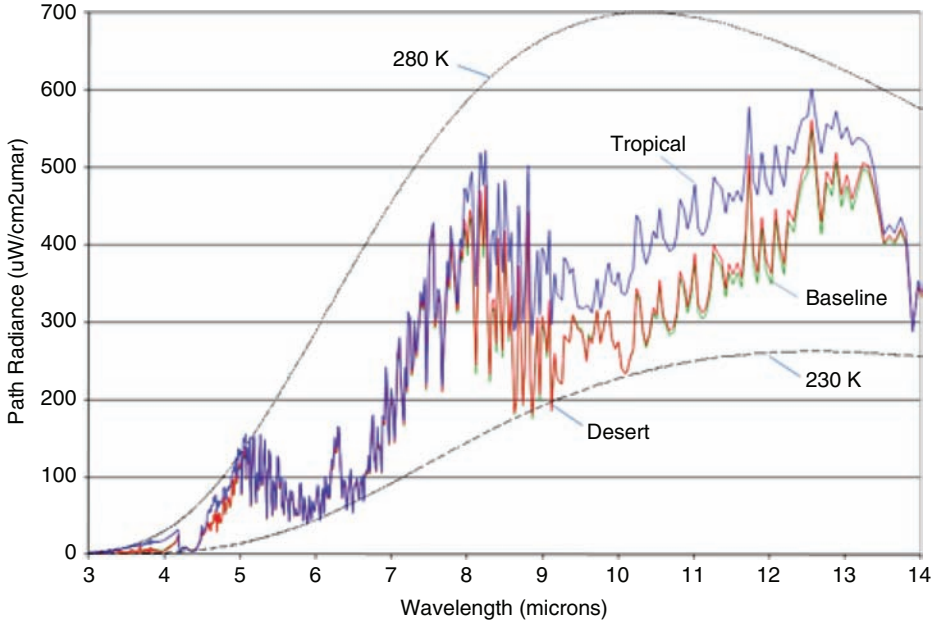

Plate 30 (Figure 17.15) Examples of path emission along a ground to space line of sight as a function of range and atmospheric conditions